

Relaxed parameter sensitivity for multiphoton quantum resonances

Hao-Lin Zhong,¹ Ke-Xiong Yan,¹ Yi-Ming Yu,¹ Shao-Wei Xu,¹
Zhi-Cheng Shi,^{1,*} Ye-Hong Chen,^{1,2,3,†} and Yan Xia^{1,2,‡}

¹*Fujian Key Laboratory of Quantum Information and Quantum Optics,
College of Physics and Information Engineering, Fuzhou University, Fuzhou 350108, China*

²*Institute of Quantum Science and Technology, Yanbian University, Yanji 133002, China*

³*Quantum Information Physics Theory Research Team,
Center for Quantum Computing, RIKEN, Wako-shi, Saitama 351-0198, Japan*

(Dated: March 11, 2026)

Multiphoton resonances demonstrate the physical significance of counter-rotating wave terms in light-matter interactions. These resonances, however, are sensitive to detuning errors, making the phenomena challenging to experimentally observe. In this manuscript, we introduce an optimization strategy to address this problem. By using an optimized parameter segmented sequence (OPSS), the robustness against detuning errors of the high-order quantum state transfers can be substantially improved. We prove the versatility of our strategy against frequency detunings by demonstrating the evolution of two specific models. In both cases, the parameter window for maintaining a high state-transfer fidelity is substantially expanded. We further analyze the output photon flux of the optimized system and, taking the three-photon resonance as an example, demonstrate that the system remains capable of generating a stable output photon flux even in the presence of detuning errors.

I. INTRODUCTION

The research of nonlinear optics is founded on the principle that a medium can respond nonlinearly to intense incident light. This principle develops a host of phenomena, which have not only found critical technological applications [1–4], but have also been demonstrated in a vast range of nonlinear media [5–8]. The profound implications of nonlinearity have inspired investigations into analogous effects in other wave-based systems, with prominent examples found in nonlinear acoustics [9], atom optics [10] and nonlinear Josephson plasma waves [11].

Analogs of such nonlinear optical effects are readily accessible in cavity quantum electrodynamics systems [12], where one or more resonator modes are coupled to a two-level atom (or an artificial atom). Just as conventional nonlinear optical effects typically require high light intensity to manifest clearly, the higher-order processes also demand a strong light-matter coupling strength [13]. This requirement is met in the ultrastrong coupling regime [13–16], where the coupling strength becomes comparable to the resonant frequencies of the system [17, 18]. Such significant coupling strength renders the counter-rotating terms non-negligible, thereby opening additional transition channels for higher-order resonant processes mediated by virtual intermediate states [15]. These high-order processes allow efficient energy exchange between the qubit and the resonator even in the large detuning regime where single-photon transitions are suppressed [19]. The existence of these

excitation-number-nonconserving pathways has excited numerous theoretical investigations, such as multiphoton oscillation [19] and multi-atom excitation [20, 21]. However, achieving such a regime is experimentally demanding, often requiring extreme system parameters or complex fabrication techniques to sufficiently enhance the coupling strength [17, 22].

In this manuscript, we investigate multi-photon resonances in the large-detuning regime with relatively weak coupling. We primarily focus on the three-photon Rabi resonance [20], involving the exchange of a qubit excitation with three photons. Furthermore, we extend our scope to the Casimir-Rabi resonance [23], where two photons are converted into three phonons. While these phenomena are of fundamental interest, the higher-order resonances in this regime are inherently sensitive to experimental errors. This is because the high-order processes rely on weak effective couplings, which makes them extremely fragile against any fluctuations in system parameters.

To overcome this fragility, we propose an optimized parameter segmented sequence (OPSS), i.e., a method inspired by composite pulse techniques [24, 25]. Originating from nuclear magnetic resonance [26, 27], composite pulses have become a standard tool for robust coherent control in diverse systems, including trapped ions [28–34], atoms [35, 36], and quantum dots [37–43].

Analogous to composite pulses that compensate for errors via varying phases or detunings [24, 44], we propose a frequency-domain strategy. Instead of a static configuration, we construct an OPSS where cavity detunings serve as dynamic control parameters optimized to render the system less sensitive to parameter fluctuations. Since analytical optimization is intractable, we employ Differential Evolution (DE) [45, 46] combined with GRAPE [47, 48] to numerically determine the ideal

* szc20147@163.com

† yehong.chen@fzu.edu.cn

‡ xia-208@163.com

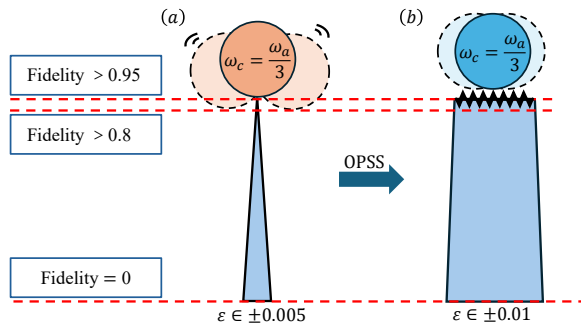


Figure 1. Schematic comparison of the robustness against detuning frequency errors for the three-photon resonance. (a) The unoptimized case. The resonance is observable only under stringent parameter conditions. The fidelity decreases to zero at a detuning error of $\epsilon = \pm 0.5\%$. Specifically, the fidelity reduces to 0.9 with a minute deviation of $\epsilon = 0.05\%$. (b) The optimized case (OPSS). The system maintains the observability of the resonance over a significantly broader error range, with fidelity degradation occurring only beyond $\epsilon = \pm 1\%$. Within this interval, the rapid oscillations maintain the fidelity in the range $[0.8, 0.9]$, ensuring the experimental visibility of the resonance.

OPSS. Our results show that the proposed OPSS method dramatically improves the tolerance to cavity frequency errors. For the standard three-photon resonance, a mere 0.5% error triggers a serious drop in fidelity from $\sim 92\%$ to $\sim 1\%$, which leads to the disappearance of the resonance signal. In contrast, our method sustains the fidelity at a high level via rapid oscillatory dynamics. Overall, this enables the resonance phenomenon to be observed within a significantly broader error range Fig.1.

Furthermore, to demonstrate the practical viability of OPSS, we extend our analysis to include environmental dissipation. By analyzing the cavity output photon flux, we observe that the optimized system yields a stable signal even in error-prone regions where the unoptimized counterpart fails to produce detectable emission.

The paper is organized as follows. Section II outlines the theoretical models and physical conditions for the three-photon and Casimir-Rabi resonances. Section III details the optimization strategy based on OPSS. Section IV analyzes the results, demonstrating how the optimized sequences render the system less sensitive to detuning errors. Finally, Section VI concludes the work.

II. THEORETICAL MODELS

A. Three-Photon Resonance

We begin by considering the quantum Rabi model ($\hbar = 1$), which describes the interaction between a two-level system (with ground state $|g\rangle$ and excited state $|e\rangle$) and a single-mode cavity resonator [20]. The Hamiltonian is

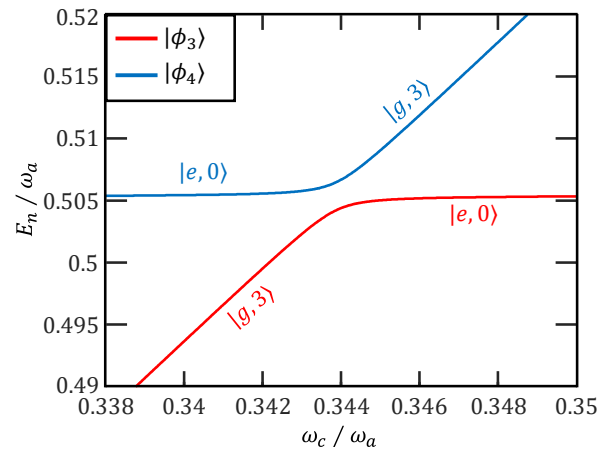


Figure 2. Eigenvalues of the third ($|\phi_3\rangle$) and fourth ($|\phi_4\rangle$) eigenstates are plotted as a function of the frequency ratio ω_c/ω_a . An avoided crossing is observed at $\omega_c/\omega_a \approx 0.334$ between the bare states $|e, 0\rangle$ and $|g, 3\rangle$. The simulation uses a coupling strength of $\lambda = 0.06 \omega_a$.

given by

$$H_R = \frac{\omega_a}{2} \sigma_z + \omega_c a^\dagger a + \lambda(a + a^\dagger) \sigma_x. \quad (1)$$

Here, ω_a and ω_c are the frequencies of the qubit and the cavity mode, respectively; a (a^\dagger) is the annihilation (creation) operator for the cavity mode, and λ is the coupling strength. The Pauli matrices are defined as $\sigma_z = |e\rangle\langle e| - |g\rangle\langle g|$ and $\sigma_x = |e\rangle\langle g| + |g\rangle\langle e|$.

In the weak-coupling regime ($\lambda \ll \omega_a, \omega_c$), an avoided crossing emerges between bare states $|e, 0\rangle$ and $|g, 3\rangle$ [49], corresponding to eigenstates $|\phi_3\rangle$ and $|\phi_4\rangle$ in Fig. 2. The sensitivity of this gap to system parameters poses a primary challenge for high-fidelity operations [49]. Near the resonance $\omega_c \approx \omega_a/3$, the dynamics are described by an effective Hamiltonian in the subspace spanned by $\{|e, 0\rangle, |g, 3\rangle\}$, derived via the time-averaging method [50] (see Appendix A).

$$H_{\text{eff}} = \frac{3\lambda^2}{2\omega_a} |e, 0\rangle\langle e, 0| + \left(-\frac{\lambda^2}{\omega_c} - \frac{9\lambda^2}{2\omega_a} \right) |g, 3\rangle\langle g, 3| - \frac{9\sqrt{6}\lambda^3}{4\omega_a^2} (|e, 0\rangle\langle g, 3| + |g, 3\rangle\langle e, 0|) = \begin{pmatrix} \frac{3\lambda^2}{2\omega_a} & -\frac{9\sqrt{6}\lambda^3}{4\omega_a^2} \\ -\frac{9\sqrt{6}\lambda^3}{4\omega_a^2} & -\frac{\lambda^2}{\omega_c} - \frac{9\lambda^2}{2\omega_a} \end{pmatrix}. \quad (2)$$

The matrix form allows us to identify the effective

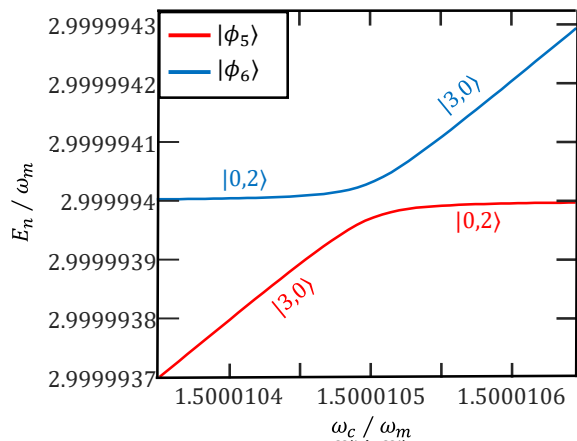


Figure 3. Eigenvalues of the fifth ($|\phi_5\rangle$) and sixth ($|\phi_6\rangle$) eigenstates are plotted as a function of the frequency ratio ω_c/ω_m . An avoided crossing is observed at $\omega_c/\omega_m \approx 1.5$ between the bare states $|2, 0\rangle$ and $|0, 3\rangle$. The minimum energy splitting is found at $\omega_c/\omega_m \approx 1.5000105$. The simulation uses a weak coupling strength of $g = 0.001 \omega_m$.

detuning Δ and the Rabi frequency Ω_{eff} as

$$\Delta = \frac{\lambda^2}{\omega_c} + \frac{6\lambda^2}{\omega_a} \quad \text{and} \quad \Omega_{\text{eff}} = -\frac{9\sqrt{6}\lambda^3}{4\omega_a^2}. \quad (3)$$

The 2×2 matrix in Eq. 2 fully describes the dynamics of the coupled two-level system, where the diagonal terms represent the AC Stark shifts of the states $\{|e, 0\rangle, |g, 3\rangle\}$ and the off-diagonal terms represent the effective coupling strength between them.

B. Casimir-Rabi Resonance in a Nonlinear Optomechanical System

As a second platform to test the generality of our method, we consider a nonlinear optomechanical system, analogous to a cavity whose resonant frequency varies with the displacement of a mechanical oscillator [51]. The Hamiltonian of Casimir-Rabi resonance is given by

$$H_{op} = \omega_c a^\dagger a + \omega_m b^\dagger b + g(a^\dagger + a)^2(b^\dagger + b). \quad (4)$$

Here, b (b^\dagger) is the annihilation (creation) operator for the mechanical mode of frequency ω_m . The parameter g represents the nonlinear coupling strength. The notation for the bare states is $|n_c, n_m\rangle$, representing n_c photons and n_m phonons.

Similar to the quantum Rabi model, this Hamiltonian illustrates a high-order multiphoton-multiphonon exchanging process when satisfying certain resonant conditions [23, 52]. The process of interest is visualized in the energy spectrum in Fig. 3, where an avoided crossing is observed between the fifth ($|\phi_5\rangle$) and sixth ($|\phi_6\rangle$) eigenstates, corresponding to a coupling between the bare states $|2, 0\rangle$ and $|0, 3\rangle$ [23].

Projecting H_s onto the basis $\{|2, 0\rangle, |0, 3\rangle\}$ yields the effective Hamiltonian describing the subspace dynamics (see Appendix A for derivation):

$$\begin{aligned} H_{\text{eff}} &= \left(2\omega_c - \frac{27g^2}{\omega_m}\right) |2, 0\rangle \langle 2, 0| \\ &+ \left(3\omega_m - \frac{6g^2}{\omega_m}\right) |0, 3\rangle \langle 0, 3| \\ &+ \frac{18\sqrt{3}g^3}{\omega_m^2} (|2, 0\rangle \langle 0, 3| + |0, 3\rangle \langle 2, 0|) \\ &= \begin{pmatrix} 2\omega_c - \frac{27g^2}{\omega_m} & \frac{18\sqrt{3}g^3}{\omega_m^2} \\ \frac{18\sqrt{3}g^3}{\omega_m^2} & 3\omega_m - \frac{6g^2}{\omega_m} \end{pmatrix}. \end{aligned} \quad (5)$$

Applying the similar procedure to the matrix of the Casimir-Rabi model, we can identify the effective detuning Δ and the effective Rabi frequency Ω_{eff} :

$$\Delta = 3\omega_m - 2\omega_c + \frac{21g^2}{\omega_m} \quad \text{and} \quad \Omega_{\text{eff}} = \frac{18\sqrt{3}g^3}{\omega_m^2}. \quad (6)$$

C. Physical Origin of Detuning Sensitivity

To elucidate the physical origin of this sensitivity, we analyze the population dynamics using the standard Rabi solution for an effective two-level system [53]. The transition probability is

$$p = \frac{\Omega_{\text{eff}}^2}{\Omega_{\text{eff}}^2 + \Delta^2} \sin^2 \left(\frac{\sqrt{\Omega_{\text{eff}}^2 + \Delta^2}}{2} t \right), \quad (7)$$

The ideal resonant conditions allows for a complete state flip ($p = 1$). However, this equation also reveals the effect introduced by the detuning error ϵ . When a small detuning error ϵ is introduced (i.e., $\omega_a \rightarrow \omega_a(1 + \epsilon)$), it induces an error in Δ , resulting in incomplete population transfer $p \neq 1$ [44].

Eq. 7 indicates that the Casimir-Rabi resonance is far more fragile than the three-photon case. Since Ω_{eff} scales cubically with the base coupling strength ($\Omega_{\text{eff}} \propto g^3, \lambda^3$), the Casimir-Rabi resonance possesses an extremely weak optomechanical coupling ($g/\omega_m \approx 0.001$), which is orders of magnitude smaller than the three-photon coupling ($\lambda/\omega_a \approx 0.06$). Therefore, even a minute detuning error ϵ causes the effective detuning term Δ to become dominant compared to the small Ω_{eff} in the Casimir system.

III. OPTIMIZATION METHODOLOGY

To counteract the pronounced parameter sensitivity identified in Sec. II, we investigate and implement a numerically robust control strategy. Our approach departs from methods like composite pulses [53]. Rather

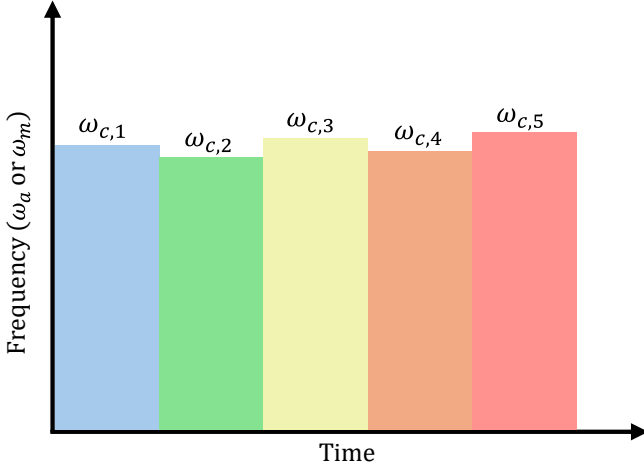


Figure 4. Schematic illustration of a set of optimizable parameters with different frequencies.

than designing controls for an effective Hamiltonian model, we directly optimize the parameters within the reduced Hamiltonian Eq. (1) or (4). Our approach replaces the single, static cavity frequency ω_c with a piecewise-constant sequence of optimized ω_c values. Critically, both the frequency values in this sequence and its total duration are numerically discovered by a hybrid DE + GRAPE optimization algorithm. This direct numerical optimization allows for the discovery of highly effective control protocols within a broader Hilbert subspace to achieve less-sensitive quantum state transfer in the studied models.

Our control scheme is defined by transforming the cavity frequency and the total evolution time into a set of optimizable parameters. The total evolution time T is divided into N segments of equal duration. During each segment k (where $k = 1, \dots, N$), the cavity frequency is held at a constant value $\omega_{c,k}$, making the Hamiltonian piecewise-static. The complete set of control parameters to be optimized is therefore the vector $\{\omega_{c,1}, \dots, \omega_{c,N}, T\}$, containing $N + 1$ variables.

To address the high computational cost of simulating the reduced Hilbert space, we employ a numerical scheme designed to simplify the optimization process. Our approach relies on the direct linear relationship between the physical control frequencies and the effective detuning Δ . This implies that optimizing the physical frequency sequence is equivalent to optimizing the Δ within the effective two-level framework. This strategy allows us to search for OPSS for the original physical model with significantly reduced computational cost.

We scanned the fidelity profile of the target state as a function of ε . The optimization range was then defined by the boundaries at which the baseline fidelity drops to a negligible value. For the three-photon resonance, the interval is set to $[-0.5\%, 0.5\%]$. For the more fragile Casimir-Rabi resonance, a much narrower interval of

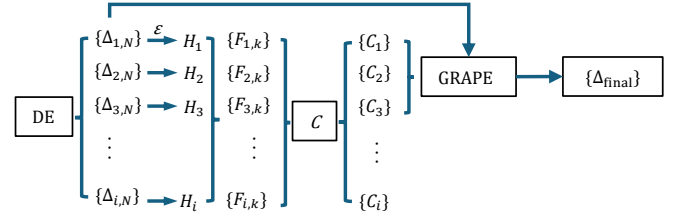


Figure 5. Schematic of the optimization workflow. The DE algorithm generates a population of $P = 100$ candidate sequences $\{\Delta_{i,N}\}$ ($i = 1, \dots, P$), where N denotes the segment number. Each sequence constructs a Hamiltonian H_i subject to detuning errors ε . The resulting fidelities $\{F_{i,k}\}$ are calculated across $M = 51$ error sample points (k) to evaluate the cost score C_i . Finally, the top-performing candidates are refined by GRAPE to yield the final optimized sequence $\{\Delta_{\text{final}}\}$. (Parameters: $w_b = 1, w_f = 500, w_r = 5$; max iterations: 1500 for DE, 3000 for GRAPE).

$[-5 \times 10^{-6}\%, 5 \times 10^{-6}\%]$ is chosen.

For the cost function evaluation, we uniformly sample M points within the defined ε range. The performance of each OPSS candidate is quantified by a composite cost function C , the minimization of which drives the optimization process (as illustrated in Fig. 5). This function is defined as a weighted sum of three distinct components:

$$C = w_b C_{\text{barrier}} + w_f C_{\text{floor}} + w_r C_{\text{robust}}. \quad (8)$$

Here, w_b , w_f , and w_r are weighting coefficients. Each component is calculated based on the set of fidelities $\{F_k\}$ ($k = 1, 2, \dots, M$), where F_k denotes the fidelity evaluated at the k -th sample point.

The first term C_{barrier} acts as the primary driving force for maximizing performance. By imposing a logarithmic penalty, it pushes every sampling point toward the theoretical ideal value:

$$C_{\text{barrier}} = \sum_{k=1}^M \log(1 - F_k).$$

The second term C_{floor} establishes a minimum performance baseline. By selectively penalizing fidelities that fall below a critical threshold F_{target} , it compels the optimizer to prioritize the rectification of worst-case regions, thereby preventing significant degradations in the fidelity profile:

$$C_{\text{floor}} = \sum_{k=1}^M [\max(0, F_{\text{target}} - F_k)]^2.$$

The final term C_{robust} directly quantifies the stability of the operation. Minimizing this standard deviation term flattens the fidelity profile, thereby enhancing the robustness of the pulse sequence against detuning errors:

$$C_{\text{robust}} = \sqrt{\frac{1}{M} \sum_{k=1}^M (F_k - \bar{F})^2},$$

Here, \bar{F} represents the mean fidelity calculated over the M sample points:

$$\bar{F} = \frac{1}{M} \sum_{k=1}^M F_k.$$

Given the system's hypersensitivity and the resulting non-convex control landscape, we employ a two-stage hybrid strategy to ensure robust convergence. In the first stage, we utilize the DE algorithm for a global search. As a population-based stochastic evolutionary algorithm, DE does not rely on gradient information but instead evolves a large number of candidates simultaneously [54, 55]. This characteristic enables DE to effectively navigate the vast parameter space and identify promising regions for the global optima, thereby avoiding local traps, while a callback function tracks and maintains an elite pool of the best candidates found. Subsequently, these top candidates serve as high-quality seeds for the second stage, where the GRAPE framework is tasked with the final high-precision refinement. GRAPE is a gradient-based optimal control algorithm known for its rapid convergence when initialized near a solution. We employ the L-BFGS-B algorithm [56, 57] as the optimization engine. This stage acts as a final sprint, rapidly converging the pre-screened candidates to the optimal solution, after which we select the result with the lowest cost function value.

In this work, we specifically investigate the performance of the OPSS for segment numbers $N = 3, 5$, and 7. We find that increasing N beyond 7 yields diminishing returns in reducing sensitivity; the marginal improvement over the $N = 7$ case does not justify the significantly higher computational cost.

IV. NUMERICAL IMPLEMENTATION

A. Parameter optimization in three-photon resonance

We begin our numerical analysis with the three-photon resonance model, establishing the unoptimized, fixed single-parameter case ($N = 1$) as the performance benchmark. To clearly demonstrate the performance enhancement achieved by our scheme, we scan the fidelity variation of the target state when applying detuning errors to both qubit frequency ω_a and cavity frequency ω_c . Specifically, the perturbed frequencies are modeled as $\omega'_a = \omega_a(1 + \varepsilon)$ and $\omega'_c = \omega_c(1 + \varepsilon)$. The results are presented in Fig. 6, with each panel corresponding to a different number of parameter segments ($N = 1, 3, 5, 7$).

For the benchmark case shown in Fig. 6(a), the high-fidelity region (yellow) is confined to an extremely narrow diagonal line. This indicates that high fidelity only exists when the parameters satisfy the strict resonance condition $\omega_a \approx 3\omega_c$. Any deviation from this stringent condition causes a severe drop. In contrast,

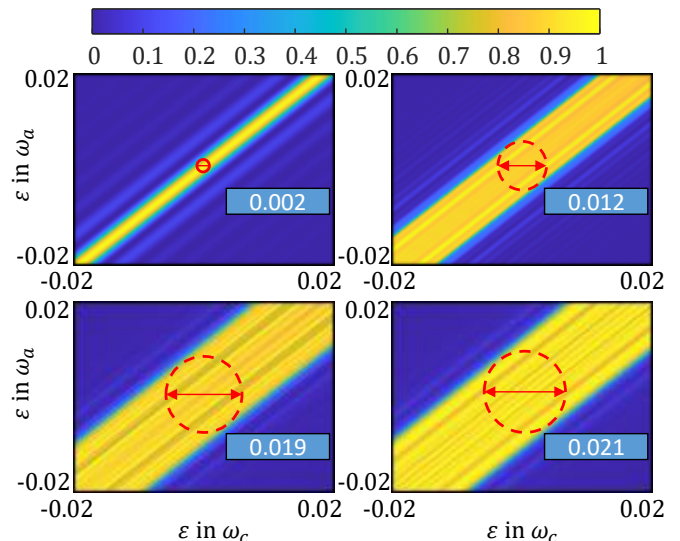


Figure 6. Fidelity landscape under detuning error ε applied to both ω_a and ω_c . Each panel shows the performance for a different number of segments: (a) $N = 1$, (b) $N = 3$, (c) $N = 5$, and (d) $N = 7$. Red dashed circles mark the robust high-fidelity radius, whose expansion with increasing N visualizes the enlarged error tolerance and reduced system sensitivity.

the implementation of the OPSS strategy successfully reshapes the line into an exceptionally broad high-fidelity plateau. We set red dashed circles to indicate the effective high-fidelity region where $F > 0.8$. As the sequence N increases, we observe a significant expansion of the radius, which directly corresponds to a broadened range of permissible errors. This achievement demonstrates that the sensitivity to detuning errors is effectively suppressed by the OPSS strategy.

To visually quantify the performance gains offered by different segment numbers N , we further investigate fidelity statistics under different levels of detuning error. To demonstrate the impact of individual parameter drifts, we fix the error on one parameter (e.g., ω_a) at $\varepsilon = 0$ while applying detuning errors to the other, then evaluate the performance within intervals centered around four distinct magnitudes: the ideal case ($\varepsilon = 0$), a tiny error regime ($\varepsilon = 0.1\%$), a moderate error regime ($\varepsilon = \pm 0.5\%$), and a large error regime ($\varepsilon = \pm 1\%$). The fidelity statistics are derived from a $\pm 10\%$ variation range surrounding each target value because the OPSS sustains the high performance via high-frequency oscillatory behavior.

The statistical results in Fig. 7 clearly demonstrate the effectiveness of the OPSS approach. For the benchmark case ($N = 1$), the system is highly sensitive to parameter deviations. According to the green bar charts in Fig. 7, even at a small error of $\varepsilon = 0.1\%$, the mean fidelity drops significantly to the $0.62 \sim 0.65$ range. As the error increases to $\varepsilon = 0.5\%$ (see the blue bar charts in Fig. 7), the fidelity collapses to negligible levels ($F < 0.1$) for both ω_a and ω_c errors.

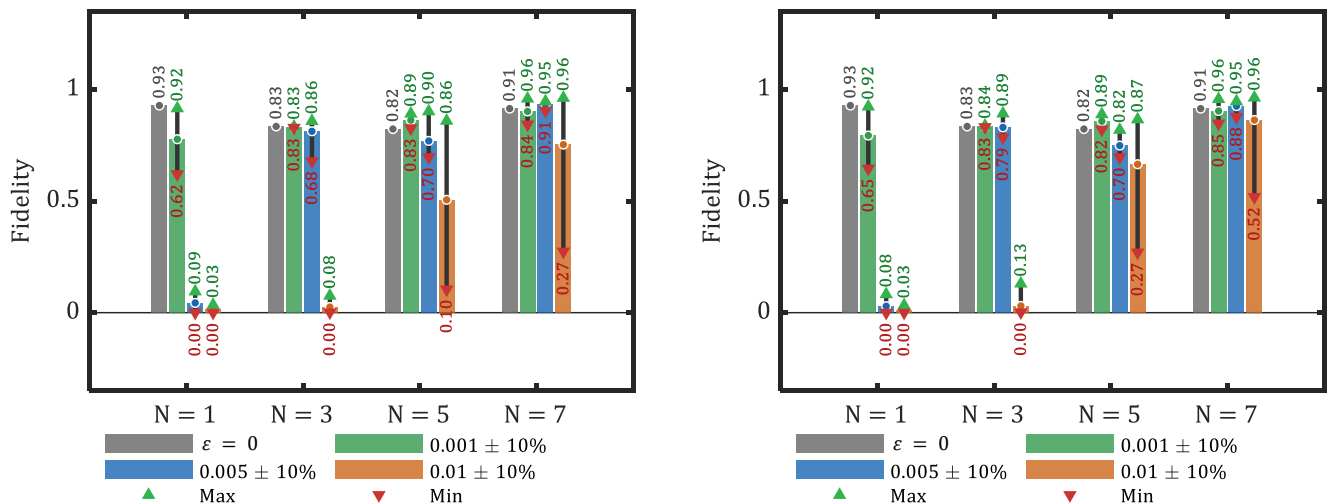


Figure 7. Performance and robustness analysis. (a) Statistical performance analysis of ε on ω_c (with ε on $\omega_a = 0$). (b) Statistical robustness analysis of ε on ω_a (with ε on $\omega_c = 0$). The height of each bar represents the mean fidelity, while the green upward triangles (\blacktriangle) and red downward triangles (\blacktriangledown) indicate the maximum and minimum fidelities within the defined ranges.

As N increases, the system maintains high fidelities over a wider error range. Both the $N = 3$ and $N = 5$ sequences successfully protect the system against small errors, maintaining fidelities above 0.8 at $\varepsilon = 0.1\%$ as shown by the green bar charts in Fig. 7. However, the $N = 3$ sequence begins to degrade when the error reaches $\varepsilon = 0.5\%$. The $N = 5$ sequence extends this protection further but eventually declines at larger error magnitudes, particularly for ω_c errors at $\varepsilon = 1\%$, where the mean fidelity drops to around 0.1.

The $N = 7$ sequence provides the most comprehensive protection. It remains stable at $\varepsilon = 0.1\%$ and maintains high mean fidelities at $\varepsilon = 0.5\%$ (0.88 for ω_a and 0.91 for ω_c). At the large error magnitude of $\varepsilon = \pm 1\%$, which is demonstrated as the orange bar charts in Fig. 7, although the average fidelity decreases, the maximum fidelity remains very high (~ 0.96) in both cases. This confirms that the OPSS strategy ensures reliable state transfer is still achievable even when the system faces significant frequency deviations, without sacrificing the stability of one parameter for the other.

B. Parameter optimization in the Casimir-Rabi Resonance

To further test the versatility of our optimization, we apply it to the Casimir-Rabi resonance, a system with a distinct physical mechanism as discussed in Sec. II. As established previously, this model represents a more stringent benchmark due to its extremely weak nonlinear coupling strength ($g/\omega_m = 0.001$), which renders it orders of magnitude more sensitive to parameter errors than the three-photon model. Our goal is to implement a robust state transfer between the initial state $|2, 0\rangle$ and

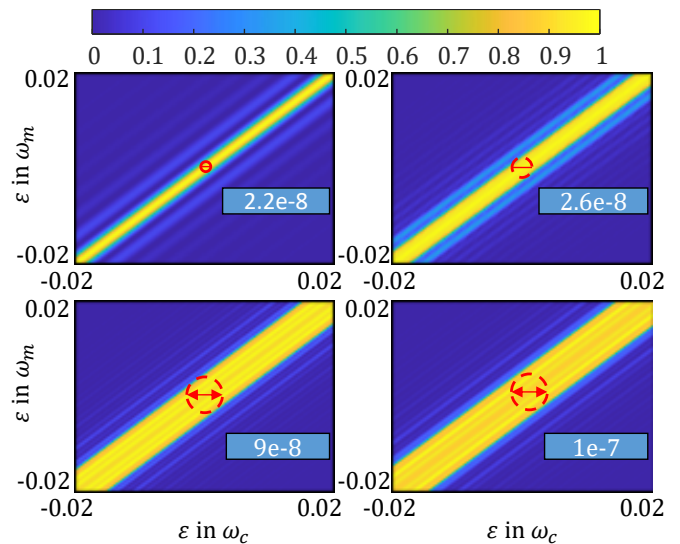


Figure 8. Fidelity landscape under detuning error ε in both ω_m and ω_c . Each panel corresponds to a different number of pulse segments: (a) $N = 1$, (b) $N = 3$, (c) $N = 5$, and (d) $N = 7$. Red dashed circles mark the robust high-fidelity radius, whose expansion with increasing N visualizes the enlarged error tolerance and reduced system sensitivity. The values of the error ε are in units of 10^{-5} .

the target state $|0, 3\rangle$.

Similar to the previous section, we scan the fidelity variation of the target state as detuning errors are applied to both the cavity frequency $\omega'_c = \omega_c(1 + \varepsilon)$ and the mechanical frequency $\omega'_m = \omega_m(1 + \varepsilon)$. The results are presented in Fig. 8, with each panel corresponding to a different number of parameter segments ($N = 1, 3, 5, 7$).

Consistent with the findings for three-photon reso-

nance, the high-fidelity region for the benchmark scheme (Fig. 8(a)) is confined to a vanishingly thin diagonal line. In contrast, our approach significantly expands this region, as visualized by the red dashed circles. The radius of these circles enlarges progressively with sequence depth, increasing from $\sim 2.2 \times 10^{-8}$ to $\sim 1 \times 10^{-7}$ for the $N = 7$ case. The success achieved on such an extreme sensitivity scale ($\sim 10^{-7}$) demonstrates that the OPSS strategy could effectively reduce the sensitivity to detuning errors in both Hamiltonian parameters.

To verify the universality of our method, we performed a similar statistical robustness analysis for the Casimir-Rabi model. The error sensitivity here operates on a much finer scale ($\sim 10^{-7}$). We evaluated performance around three distinct error magnitudes: 0.3×10^{-7} , 0.6×10^{-7} , and 1.0×10^{-7} .

The results in Fig. 9 are similar to the trends observed in the three-photon resonance. The benchmark $N = 1$ pulse is extremely fragile; even a minor error of $\varepsilon = 0.3 \times 10^{-7}$ causes the mean fidelity to drop to ~ 0.45 . Increasing the segment number N effectively broadens the tolerance window. The $N = 5$ sequence maintains robust performance ($F > 0.85$) up to $\varepsilon = 0.6 \times 10^{-7}$ but eventually degrades at larger magnitudes. The $N = 7$ sequence delivers the most comprehensive protection. Notably, at the error magnitude of $\varepsilon = 1.0 \times 10^{-7}$, the maximum fidelity remains remarkably high (> 0.87) for both parameters. This confirms that the OPSS strategy successfully preserves high-fidelity solutions even in highly sensitive quantum systems.

C. Output Photon Flux

In this section, we employ the master equation to investigate the output photon flux of the cavity. We consider the three-photon resonance as an example, a system in which the artificial atom and the cavity field are coupled to separate baths. It is assumed that the temperature of the baths is zero. By employing the Born-Markov approximation, the master equation [58–60] for the reduced density matrix of the system, $\rho(t)$, in the Schrödinger picture can be written as

$$\frac{d\rho(t)}{dt} = -i[H(t), \rho(t)] + \kappa\mathcal{D}[X_1]\rho + \gamma\mathcal{D}[X_2]\rho. \quad (9)$$

Here, $H(t)$ is the total system Hamiltonian given by Eq. (1), κ represents the photon decay rate, and γ denotes the atomic relaxation rate. The operators X_1 and X_2 are defined by

$$X_1 = \sum_{E_n > E_m} \langle \psi_m | (a + a^\dagger) | \psi_n \rangle | \psi_m \rangle \langle \psi_n |, \quad (10)$$

$$X_2 = \sum_{E_n > E_m} \langle \psi_m | \sigma_x | \psi_n \rangle | \psi_m \rangle \langle \psi_n |. \quad (11)$$

X_1 and X_2 are the jump operators, describing transitions from high-energy eigenstates to low-energy eigenstates.

The eigenstates $|\psi_n\rangle$ are the instantaneous eigenstates of the Hamiltonian, satisfying $H(t)|\psi_n\rangle = E_n(t)|\psi_n\rangle$. The standard Lindblad superoperator \mathcal{D} is defined by

$$\mathcal{D}[O]\rho = \frac{1}{2} (2O\rho O^\dagger - O^\dagger O\rho - \rho O^\dagger O). \quad (12)$$

For the three-photon Rabi resonance, the output photon flux rate [59, 60] from the cavity field is defined by

$$\Phi_{\text{out}}(t) = \kappa \text{Tr}[\rho(t) X_1^\dagger X_1]. \quad (13)$$

To strictly evaluate the robustness of the scheme under realistic noise conditions, we calculate the time-dependent output photon flux using the global master equation approach. By mapping the output photon flux Φ_{out} against the detuning error ε , we demonstrate the dynamical behaviors of the three-photon resonance in Fig. 10. We perform a comparative analysis of the output photon flux dynamics for the standard ($N = 1$) and optimized ($N = 7$) schemes in the presence of detuning errors. For clarity, the time evolution is plotted against the normalized ratio t/T , where T denotes the total pulse duration. The duration for the unoptimized single-pulse case is $T_{N=1} \approx 1320 \omega_c^{-1}$, whereas the OPSS requires a much longer duration of $T_{N=7} \approx 9440 \omega_c^{-1}$.

As observed in the unoptimized three-photon resonance case in Figs. 10(a) and 10(c), regardless of whether the error ε is applied to ω_a or ω_c , a significant output photon flux at the end of the evolution is confined to a narrow interval of $\varepsilon \in [-0.5\%, 0.5\%]$. This is consistent with our previous results shown in Fig. 6(a). In contrast, for the optimized $N = 7$ case in Figs. 10(b) and 10(d), a stable output photon flux is maintained at the end of the evolution across a much wider range of $\varepsilon \in [-1\%, 1\%]$. This demonstrates that the three-photon resonance can be maintained with our optimization strategy even in the presence of coupling to the environment.

For the case of Casimir-Rabi resonance, the master equation remains identical to Eq. (9). The Hamiltonian is replaced by Eq. (4), where γ represents the phonon decay rate. While X_1 remains unchanged, X_2 is defined as

$$X_2 = \sum_{E_n > E_m} \langle \psi_m | (b + b^\dagger) | \psi_n \rangle | \psi_m \rangle \langle \psi_n |. \quad (14)$$

V. EXPERIMENTAL IMPLEMENTATION

To experimentally verify our theoretical predictions, we propose utilizing two distinct physical architectures tailored to the specific spectral and coupling requirements of the three-photon and Casimir-Rabi dynamics.

For the three-photon resonance, a superconducting circuit QED system is a promising candidate. We consider a fluxonium qubit coupled to a frequency-tunable transmission line resonator [61, 62]. The

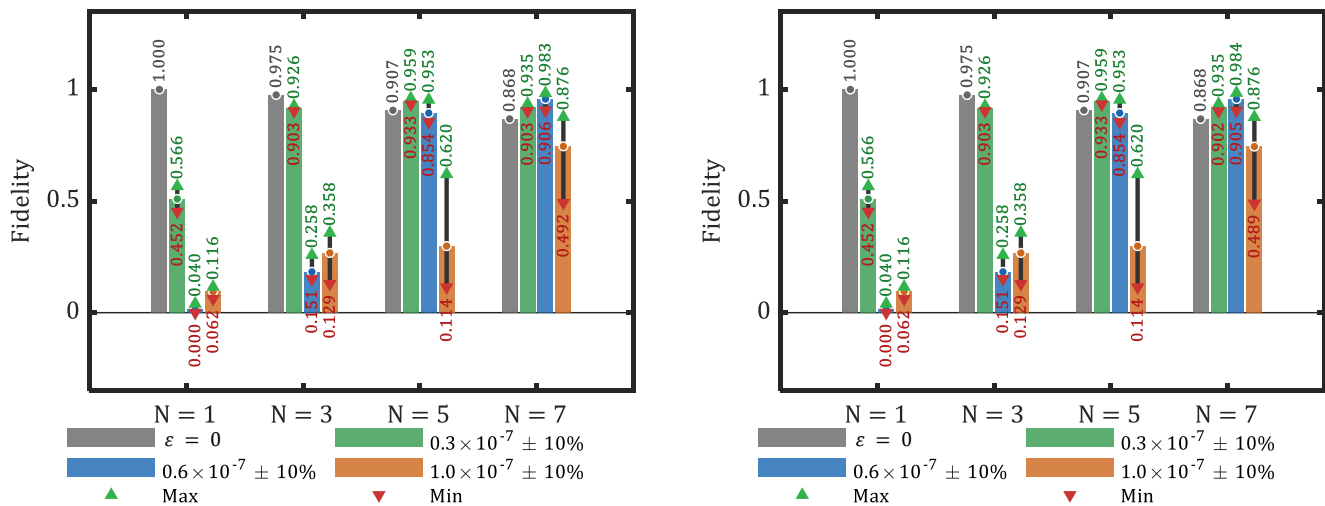


Figure 9. Performance and robustness analysis. (a) Statistical performance analysis of ε on ω_m (with ε on $\omega_c = 0$). (b) Statistical robustness analysis of ε on ω_c (with ε on $\omega_m = 0$). The height of each bar represents the mean fidelity, while the green upward triangles (▲) and red downward triangles (▼) indicate the maximum and minimum fidelities within the defined ranges.

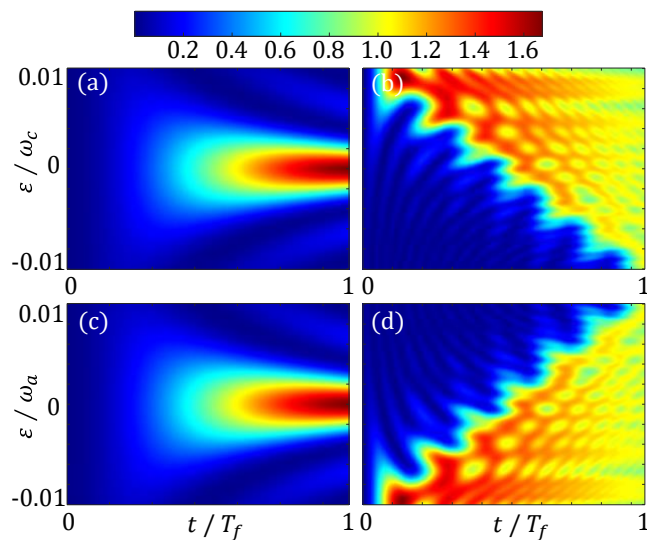


Figure 10. Differential output photon flux landscapes for the three-photon resonance model. The decay rates are set to $\kappa = \gamma = 0.00006$. The flux values are scaled by 10^{-4} . (a) and (b) ε on ω_a . (c) and (d) ε on ω_c .

fluxonium circuit provides the necessary giant anharmonicity to resolve higher-order transitions, while the resonator frequency ω_c can be continuously tuned via a SQUID array termination [63]. This allows for the precise in-situ adjustment of the cavity mode to satisfy the three-photon resonance condition $\omega_q \approx 3\omega_c$. Typical experimental parameters for such setups involve qubit and cavity frequencies in the microwave domain ($\omega_{q,c}/2\pi \approx 4\text{--}8$ GHz) with tunable bandwidths exceeding 1 GHz [64], ensuring the system can be stabilized at the targeted triple-frequency optimization point.

The Casimir-Rabi oscillations can be effectively realized in a superconducting circuit architecture where a DC SQUID is integrated into a coplanar microwave cavity. In this setup, a segment of the SQUID loop functions as a mechanical resonator, establishing an effective optomechanical coupling via the flux-dependent Josephson inductance [17, 18]. By modulating the external magnetic flux, the effective cavity frequency is dynamically tuned to satisfy the resonance conditions necessary for the third-order phonon-photon interaction. Furthermore, considering the ultra-high quality factors of state-of-the-art nanomechanical resonators ($Q > 10^{10}$) [65] and superconducting cavities [66], this scheme is well within the reach of current experimental capabilities.

VI. CONCLUSION

In conclusion, we have introduced and numerically validated a powerful optimization strategy to address the pronounced parameter sensitivity inherent in quantum systems governed by high-order interactions. By using OPSS, our method directly reduces the sensitivity of the three-photon resonance and the Casimir-Rabi resonance against detuning errors, expanding the high-fidelity operational window by an order of magnitude.

The consistent success across two systems with disparate physical mechanisms and sensitivity scales demonstrates the versatility and capability of our numerical discovery method. In contrast to traditional techniques that rely on simplified models [53] and analytical constructions, our strategy offers a more flexible and powerful paradigm for designing robust controls for complex quantum dynamics processes.

This paves the way for harnessing high-order resonant phenomena for applications in quantum information processing and precision measurement in realistic, noisy environments.

Looking forward, this optimization framework can be extended in several promising directions. An immediate next step is to incorporate decoherence effects explicitly into the cost function, aiming to identify an optimal trade-off between error robustness and finite coherence times in open quantum systems [53, 67]. Moreover, the methodology is readily applicable to other physical platforms grappling with similar parameter uncertainties, such as optimizing quantum gate operations in solid-state spin systems [68] or trapped ions [69]. We believe the numerical blueprints provided in this study will motivate future experimental efforts to achieve ultra-precise and robust control of high-order quantum processes.

ACKNOWLEDGMENTS

Y.-H.C. was supported by the National Natural Science Foundation of China (Grant Nos. 12304390 and 12574386), the Fujian 100 Talents Program, and the Fujian Minjiang Scholar Program. Z.-C.S. was supported by the National Natural Science Foundation of China (Grant No. 62571129) and the Natural Science Foundation of Fujian Province (Grant No. 2025J01456). Y.X. was supported by the National Natural Science Foundation of China (Grant Nos. 11575045 and 62471143), the Natural Science Funds for Distinguished Young Scholar of Fujian Province (Grant No. 2020J06011), and the Project from Fuzhou University (Grant No. JG202001-2).

DATA AVAILABILITY

The data used for obtaining the presented numerical results as well as for generating the plots is available on request. Please refer to yehong.chen@fzu.edu.cn.

Appendix A: DERIVATION OF THE EFFECTIVE HAMILTONIAN

1. THE THREE-PHOTON RESONANCE

We begin with the quantum Rabi model in the interaction picture with respect to the free Hamiltonian $\hat{H}_0 = \frac{1}{2}\omega_a\hat{\sigma}_z + \omega_c\hat{a}^\dagger\hat{a}$. The interaction Hamiltonian ($\hbar = 1$) is given by

$$\hat{H}_I = \lambda[\hat{a}e^{i(\omega_a - \omega_c)t} + \hat{a}^\dagger e^{i(\omega_a + \omega_c)t}]\hat{\sigma}_+ + \text{H.c.}, \quad (\text{A1})$$

where λ is the atom-cavity coupling rate, \hat{a} (\hat{a}^\dagger) is the annihilation (creation) operator for the cavity mode of frequency ω_c , and ω_a is the atomic transition frequency.

The Pauli operators are defined as $\hat{\sigma}_z = |e\rangle\langle e| - |g\rangle\langle g|$, $\hat{\sigma}_+ = |e\rangle\langle g|$, and $\hat{\sigma}_- = |g\rangle\langle e|$.

Under the three-photon resonance condition $\omega_a = 3\omega_c$, the interaction Hamiltonian in Eq. (A1) can be expressed in terms of its harmonic components:

$$\hat{H}_I = \lambda(\hat{a}e^{2i\omega_c t} + \hat{a}^\dagger e^{4i\omega_c t})\hat{\sigma}_+ + \text{H.c.} \quad (\text{A2})$$

From this expression, we can derive the effective Hamiltonian using the time-averaging method. According to this method, the second-order time-independent effective Hamiltonian is given by the general formula:

$$\hat{H}_{\text{eff}}^{(2)} = \sum_m \frac{1}{\omega_m} [\hat{h}_m, \hat{h}_m^\dagger], \quad (\text{A3})$$

where \hat{h}_m are the operator components of \hat{H}_I oscillating at frequencies ω_m . For the Hamiltonian in Eq. (A2), we can identify its harmonic components and, by substituting them into Eq. (A3), obtain the second-order effective Hamiltonian:

$$\hat{H}_{\text{eff}}^{(2)} = \frac{\lambda^2}{4\omega_c} [-(3\hat{a}^\dagger\hat{a} + 2)\hat{\sigma}_+\hat{\sigma}_- - (3\hat{a}^\dagger\hat{a} + 1)\hat{\sigma}_-\hat{\sigma}_+]. \quad (\text{A4})$$

Similarly, following the standard formalism [50, 58], the general formula for the third-order term is given by

$$\begin{aligned} \hat{H}_{\text{eff}}^{(3)}(t) = \sum_{l,m,n} \left\{ \frac{1}{\omega_n(\omega_n - \omega_m)} \left[\hat{h}_l \hat{h}_m^\dagger \hat{h}_n e^{i(\omega_l - \omega_m + \omega_n)t} \right. \right. \\ + \hat{h}_l^\dagger \hat{h}_m \hat{h}_n e^{i(-\omega_l + \omega_m + \omega_n)t} \\ + \hat{h}_l \hat{h}_m \hat{h}_n^\dagger e^{i(\omega_l + \omega_m - \omega_n)t} \\ \left. \left. + \hat{h}_l^\dagger \hat{h}_m^\dagger \hat{h}_n e^{i(-\omega_l - \omega_m + \omega_n)t} \right] \right. \\ \left. + \frac{1}{\omega_n(\omega_n + \omega_m)} \left[\hat{h}_l \hat{h}_m^\dagger \hat{h}_n^\dagger e^{i(\omega_l - \omega_m - \omega_n)t} \right. \right. \\ \left. \left. + \hat{h}_l^\dagger \hat{h}_m \hat{h}_n^\dagger e^{i(-\omega_l + \omega_m - \omega_n)t} \right] \right\}. \quad (\text{A5}) \end{aligned}$$

which leads to the following time-averaged third-order correction:

$$\hat{H}_{\text{eff}}^{(3)} = -\frac{\lambda^3}{4\omega_c^2} [(\hat{a}^\dagger)^3\hat{\sigma}_- + \hat{a}^3\hat{\sigma}_+]. \quad (\text{A6})$$

To obtain a concrete matrix representation, we project these operators onto the resonant two-level subspace spanned by the states $\{|e, 0\rangle, |g, 3\rangle\}$. First, we evaluate the matrix elements of $\hat{H}_{\text{eff}}^{(2)}$. This operator is diagonal in this basis. The top-left element is $\langle e, 0 | \hat{H}_{\text{eff}}^{(2)} | e, 0 \rangle$ ($n = 0$):

$$(\hat{H}_{\text{eff}}^{(2)})_{11} = \frac{\lambda^2}{4\omega_c} [-(3(0) + 2)] = -\frac{\lambda^2}{2\omega_c}. \quad (\text{A7})$$

The bottom-right element is $\langle g, 3 | \hat{H}_{\text{eff}}^{(2)} | g, 3 \rangle$ ($n = 3$):

$$(\hat{H}_{\text{eff}}^{(2)})_{22} = \frac{\lambda^2}{4\omega_c} [-(3(3) + 1)] = -\frac{5\lambda^2}{2\omega_c}. \quad (\text{A8})$$

Next, we evaluate the matrix elements of $\hat{H}_{\text{eff}}^{(3)}$, which provides the off-diagonal coupling. The off-diagonal term is given by $\langle e, 0 | \hat{H}_{\text{eff}}^{(3)} | g, 3 \rangle$:

$$\begin{aligned} (\hat{H}_{\text{eff}}^{(3)})_{12} &= \langle e, 0 | \left(-\frac{\lambda^3}{4\omega_c^2} \right) \hat{a}^3 \hat{\sigma}_+ | g, 3 \rangle \\ &= -\frac{\lambda^3}{4\omega_c^2} \langle e, 0 | \hat{a}^3 | e, 3 \rangle \\ &= -\frac{\lambda^3}{4\omega_c^2} \langle e, 0 | \sqrt{3 \cdot 2 \cdot 1} | e, 0 \rangle = -\frac{\sqrt{6}\lambda^3}{4\omega_c^2}. \end{aligned} \quad (\text{A9})$$

The other off-diagonal element $(\hat{H}_{\text{eff}}^{(3)})_{21}$ is its Hermitian conjugate and has the same value.

Finally, the total effective Hamiltonian is the sum $\hat{H}_{\text{eff}} = \hat{H}_{\text{eff}}^{(2)} + \hat{H}_{\text{eff}}^{(3)}$. Its matrix representation in the basis $\{|e, 0\rangle, |g, 3\rangle\}$ is

$$\hat{H}_{\text{eff}} = \begin{pmatrix} -\frac{\lambda^2}{2\omega_c} & -\frac{\sqrt{6}\lambda^3}{4\omega_c^2} \\ \frac{\sqrt{6}\lambda^3}{4\omega_c^2} & -\frac{5\lambda^2}{2\omega_c} \end{pmatrix}. \quad (\text{A10})$$

The effective Hamiltonian in Eq. (A10) is derived in the interaction picture, meaning its diagonal elements represent the energy shifts (AC Stark shifts) caused by the interaction. To obtain the total Hamiltonian in the laboratory frame (Schrödinger picture), we must add back the contribution from the free Hamiltonian, \hat{H}_0 .

$$\hat{H}_S = \hat{H}_0 + \hat{H}_{\text{eff}}. \quad (\text{A11})$$

We compute the matrix elements of \hat{H}_0 in our basis. Applying the resonance condition $\omega_a = 3\omega_c$, this simplifies to $\frac{\omega_a}{2}$. Thus, \hat{H}_0 contributes a constant energy offset to both states.

By adding this diagonal contribution to Eq. (A10), we arrive at the final effective Hamiltonian in the Schrödinger picture:

$$\hat{H}_S = \begin{pmatrix} \frac{\omega_a}{2} - \frac{\lambda^2}{2\omega_c} & -\frac{\sqrt{6}\lambda^3}{4\omega_c^2} \\ -\frac{\sqrt{6}\lambda^3}{4\omega_c^2} & \frac{\omega_a}{2} - \frac{5\lambda^2}{2\omega_c} \end{pmatrix}. \quad (\text{A12})$$

2. The Casimir-Rabi Resonance

To analyze the system dynamics, we transform the Hamiltonian into the interaction picture with respect

to the free Hamiltonian $\hat{H}_0 = \omega_c \hat{a}^\dagger \hat{a} + \omega_m \hat{b}^\dagger \hat{b}$. In this picture, the interaction Hamiltonian $\hat{H}_I(t)$ can be expanded to explicitly show its harmonic components. Its full, unapproximated form is given by

$$\begin{aligned} \hat{H}_I(t) &= g \left[(\hat{a}^\dagger)^2 \hat{b}^\dagger e^{i(2\omega_c + \omega_m)t} + (\hat{a}^\dagger)^2 \hat{b} e^{i(2\omega_c - \omega_m)t} \right. \\ &\quad \left. + (2\hat{a}^\dagger \hat{a} + 1) \hat{b}^\dagger e^{i\omega_m t} \right] + \text{H.c.} \end{aligned} \quad (\text{A13})$$

According to Eq. (A3), the second-order $\hat{H}_{\text{eff}}^{(2)}$ with the resonance condition $3\omega_m = 2\omega_c$ is given by

$$\begin{aligned} \hat{H}_{\text{eff}}^{(2)} &= \frac{g^2}{\omega_m} \left[\frac{1}{4} \left((\hat{a}^\dagger)^2 \hat{a}^2 \hat{b}^\dagger \hat{b} - \hat{b} \hat{b}^\dagger \hat{a}^2 (\hat{a}^\dagger)^2 \right) \right. \\ &\quad \left. + \frac{1}{2} \left((\hat{a}^\dagger)^2 \hat{a}^2 \hat{b} \hat{b}^\dagger - \hat{b}^\dagger \hat{b} \hat{a}^2 (\hat{a}^\dagger)^2 \right) \right. \\ &\quad \left. - (2\hat{a}^\dagger \hat{a} + 1)^2 \right]. \end{aligned} \quad (\text{A14})$$

Similarly, we derive the third-order effective Hamiltonian, $\hat{H}_{\text{eff}}^{(3)}$, by applying the general formula from Eq. (A5). Instead of presenting its full and complex operator form, we focus on its matrix representation within the resonant subspace spanned by $\{|2, 0\rangle, |0, 3\rangle\}$. The evaluation of the off-diagonal matrix element $\langle 2, 0 | \hat{H}_{\text{eff}}^{(3)} | 0, 3 \rangle$ yields the following compact matrix:

$$\hat{H}_{\text{eff}}^{(3)} = \frac{18\sqrt{3}g^3}{\omega_m^2} \begin{pmatrix} 0 & 1 \\ 1 & 0 \end{pmatrix}. \quad (\text{A15})$$

Combining the second-order and the third-order terms, we obtain the full effective Hamiltonian in the interaction picture for the resonant subspace, $\hat{H}_{\text{eff}} = \hat{H}_{\text{eff}}^{(2)} + \hat{H}_{\text{eff}}^{(3)}$:

$$\hat{H}_{\text{eff}} = \begin{pmatrix} -\frac{27g^2}{\omega_m} & \frac{18\sqrt{3}g^3}{\omega_m^2} \\ \frac{18\sqrt{3}g^3}{\omega_m^2} & -\frac{6g^2}{\omega_m} \end{pmatrix}. \quad (\text{A16})$$

To obtain the total Hamiltonian in the Schrödinger picture, we must add back the contribution from the free Hamiltonian, $\hat{H}_0 = \omega_c \hat{a}^\dagger \hat{a} + \omega_m \hat{b}^\dagger \hat{b}$. Its matrix elements in the basis $\{|2, 0\rangle, |0, 3\rangle\}$ are given by $E_1 = \langle 2, 0 | \hat{H}_0 | 2, 0 \rangle = 2\omega_c$ and $E_2 = \langle 0, 3 | \hat{H}_0 | 0, 3 \rangle = 3\omega_m$.

The final effective Hamiltonian in the Schrödinger picture, $\hat{H}_S = \hat{H}_0 + \hat{H}_{\text{eff}}$, is therefore:

$$\hat{H}_S = \begin{pmatrix} 2\omega_c - \frac{27g^2}{\omega_m} & \frac{18\sqrt{3}g^3}{\omega_m^2} \\ \frac{18\sqrt{3}g^3}{\omega_m^2} & 3\omega_m - \frac{6g^2}{\omega_m} \end{pmatrix}. \quad (\text{A17})$$

The diagonal elements of this matrix represent the absolute energies of the dressed states, while the off-diagonal terms describe the effective coupling between them.

- [1] P. A. Lindsay, *Introduction to Quantum Electronics* (Pitman, London, 1975).
- [2] S. Kielich, *Molecular Nonlinear Optics* (Nauka, Moscow, 1981).
- [3] Y. R. Shen, *The Principles of Nonlinear Optics* (Wiley, New York, 1984).
- [4] R. W. Boyd, *Nonlinear Optics*, 3rd ed. (Elsevier, Amsterdam, 2008).
- [5] L. Liu, L. Zhao, X. Zhou, and X. Wang, Recent progress in the development of KBe₂BO₃F₂: a deep-uv nonlinear optical crystal, *Appl. Phys. B* **128**, 17 (2022).
- [6] J. M. Dudley, G. Genty, and S. Coen, Supercontinuum generation in photonic crystal fiber, *Rev. Mod. Phys.* **78**, 1135 (2006).
- [7] J. N. Acharyya and G. V. Prakash, Nonlinear optical dispersion and higher-order effects in bulk and wavelength-ordered photonic materials, *Optik* **247**, 167944 (2021).
- [8] V. Kumar, Linear and nonlinear optical properties of graphene: A review, *J. Electron. Mater.* **50**, 3773 (2021).
- [9] M. F. Hamilton and D. T. Blackstock, eds., *Nonlinear Acoustics* (Springer Nature Switzerland, Cham, 2024).
- [10] S. L. Rolston and W. D. Phillips, Nonlinear and quantum atom optics, *Nature* **416**, 219 (2002).
- [11] S. Savel'ev, A. L. Rakhmanov, V. A. Yampol'skii, and F. Nori, Analogues of nonlinear optics using terahertz Josephson plasma waves in layered superconductors, *Nat. Phys.* **2**, 521 (2006).
- [12] A. Blais, A. L. Grimsmo, S. M. Girvin, and A. Wallraff, Circuit quantum electrodynamics, *Rev. Mod. Phys.* **93**, 025005 (2021).
- [13] T. Niemczyk, F. Deppe, H. Huebl, E. P. Menzel, F. Hocke, M. J. Schwarz, J. J. Garcia-Ripoll, D. Zueco, T. Hümmer, E. Solano, A. Marx, and R. Gross, Circuit quantum electrodynamics in the ultrastrong-coupling regime, *Nat. Phys.* **6**, 772 (2010).
- [14] A. Fedorov, A. K. Feofanov, P. Macha, P. Forn-Díaz, C. J. P. M. Harmans, and J. E. Mooij, Strong coupling of a quantum oscillator to a flux qubit at its symmetry point, *Phys. Rev. Lett.* **105**, 060503 (2010).
- [15] P. Forn-Díaz, J. Lisenfeld, D. Marcos, J. J. García-Ripoll, E. Solano, C. J. P. M. Harmans, and J. E. Mooij, Observation of the Bloch-Siegert shift in a qubit-oscillator system in the ultrastrong coupling regime, *Phys. Rev. Lett.* **105**, 237001 (2010).
- [16] P. Forn-Díaz, G. Romero, C. J. P. M. Harmans, E. Solano, and J. E. Mooij, Broken selection rule in the quantum Rabi model, *Sci. Rep.* **6**, 26720 (2016).
- [17] A. Frisk Kockum, A. Miranowicz, S. De Liberato, S. Savasta, and F. Nori, Ultrastrong coupling between light and matter, *Nat. Rev. Phys.* **1**, 19 (2019).
- [18] P. Forn-Díaz, L. Lamata, E. Rico, J. Kono, and E. Solano, Ultrastrong coupling regimes of light-matter interaction, *Rev. Mod. Phys.* **91**, 025005 (2019).
- [19] L. Garziano, R. Stassi, V. Macrì, A. F. Kockum, S. Savasta, and F. Nori, Multiphoton quantum Rabi oscillations in ultrastrong cavity QED, *Phys. Rev. A* **92**, 063830 (2015).
- [20] K. K. W. Ma and C. K. Law, Three-photon resonance and adiabatic passage in the large-detuning Rabi model, *Phys. Rev. A* **92**, 023842 (2015).
- [21] L. Garziano, V. Macrì, R. Stassi, O. Di Stefano, F. Nori, and S. Savasta, One photon can simultaneously excite two or more atoms, *Phys. Rev. Lett.* **117**, 043601 (2016).
- [22] N. S. Mueller, E. B. Barros, and S. Reich, Ultrastrong light-matter coupling in materials (2025), [arXiv:2505.06373](https://arxiv.org/abs/2505.06373) [physics.optics].
- [23] K.-X. Yan, Y. Qiu, Y. Xiao, J. Song, Y.-H. Chen, and Y. Xia, Spontaneous emission in Casimir-Rabi oscillations through a weak optomechanical coupling, *Opt. Express* **33**, 39283 (2025).
- [24] E. Kyoseva, H. Greener, and H. Suchowski, Detuning-modulated composite pulses for high-fidelity robust quantum control, *Phys. Rev. A* **100**, 032333 (2019).
- [25] B. T. Torosov and N. V. Vitanov, Robust high-fidelity coherent control of two-state systems by detuning pulses, *Phys. Rev. A* **99**, 013424 (2019).
- [26] R. Freeman, *Spin Choreography: Basic Steps in High Resolution NMR* (Oxford University Press, Oxford, 1998).
- [27] M. H. Levitt, Composite pulses, *Encycl. Magn. Reson.*, emrstm0086 (2007).
- [28] H. Häffner, C. F. Roos, and R. Blatt, Quantum computing with trapped ions, *Phys. Rep.* **469**, 155 (2008).
- [29] T. Monz, K. Kim, W. Hänsel, M. Riebe, A. S. Villar, P. Schindler, M. Chwalla, M. Hennrich, and R. Blatt, Realization of the quantum Toffoli gate with trapped ions, *Phys. Rev. Lett.* **102**, 040501 (2009).
- [30] C. M. Shappert, J. T. Merrill, K. R. Brown, J. M. Amini, C. Volin, S. C. Doret, H. Hayden, C.-S. Pai, K. R. Brown, and A. W. Harter, Spatially uniform single-qubit gate operations with near-field microwaves and composite pulse compensation, *New J. Phys.* **15**, 083053 (2013).
- [31] N. Timoney, V. Elman, S. Glaser, C. Weiss, M. Johanning, W. Neuhauser, and C. Wunderlich, Error-resistant single-qubit gates with trapped ions, *Phys. Rev. A* **77**, 052334 (2008).
- [32] S. Gulde, M. Riebe, G. P. T. Lancaster, C. Becher, J. Eschner, H. Häffner, F. Schmidt-Kaler, I. L. Chuang, and R. Blatt, Implementation of the Deutsch-Jozsa algorithm on an ion-trap quantum computer, *Nature* **421**, 48 (2003).
- [33] G. Zarantonello, H. Hahn, J. Morgner, M. Schulte, A. Bautista-Salvador, R. F. Werner, K. Hammerer, and C. Ospelkaus, Robust and resource-efficient microwave near-field entangling ⁹Be⁺ gate, *Phys. Rev. Lett.* **123**, 260503 (2019).
- [34] E. Mount, C. Kabytayev, S. Crain, R. Harper, S.-Y. Baek, G. Vrijsen, S. T. Flammia, K. R. Brown, P. Maunz, and J. Kim, Error compensation of single-qubit gates in a surface-electrode ion trap using composite pulses, *Phys. Rev. A* **92**, 060301 (2015).
- [35] W. Rakreungdet, J. H. Lee, K. F. Lee, B. E. Mischuck, E. Montano, and P. S. Jessen, Accurate microwave control and real-time diagnostics of neutral-atom qubits, *Phys. Rev. A* **79**, 022316 (2009).
- [36] G. Demeter, Composite pulses for high-fidelity population inversion in optically dense, inhomogeneously broadened atomic ensembles, *Phys. Rev. A* **93**, 023830 (2016).
- [37] X. Wang, L. S. Bishop, J. P. Kestner, E. Barnes, K. Sun,

- and S. Das Sarma, Composite pulses for robust universal control of singlet-triplet qubits, *Nat. Commun.* **3**, 997 (2012).
- [38] K. Eng, T. D. Ladd, A. Smith, M. G. Borselli, A. A. Kiselev, B. H. Fong, K. S. Holabird, T. M. Hazard, B. Huang, P. W. Deelman, I. Milosavljevic, A. E. Schmitz, R. S. Ross, M. F. Gyure, and A. T. Hunter, Isotopically enhanced triple-quantum-dot qubit, *Sci. Adv.* **1**, e1500214 (2015).
- [39] G. T. Genov, D. Schraft, N. V. Vitanov, and T. Halfmann, Arbitrarily accurate pulse sequences for robust dynamical decoupling, *Phys. Rev. Lett.* **118**, 133202 (2017).
- [40] X. Wang, L. S. Bishop, E. Barnes, J. P. Kestner, and S. Das Sarma, Robust quantum gates for singlet-triplet spin qubits using composite pulses, *Phys. Rev. A* **89**, 022310 (2014).
- [41] C. Zhang, R. E. Throckmorton, X.-C. Yang, X. Wang, E. Barnes, and S. Das Sarma, Randomized benchmarking of barrier versus tilt control of a singlet-triplet qubit, *Phys. Rev. Lett.* **118**, 216802 (2017).
- [42] J. P. Kestner, X. Wang, L. S. Bishop, E. Barnes, and S. Das Sarma, Noise-resistant control for a spin qubit array, *Phys. Rev. Lett.* **110**, 140502 (2013).
- [43] G. T. Hickman, X. Wang, J. P. Kestner, and S. Das Sarma, Dynamically corrected gates for an exchange-only qubit, *Phys. Rev. B* **88**, 161303 (2013).
- [44] B. T. Torosov and N. V. Vitanov, Smooth composite pulses for high-fidelity quantum information processing, *Phys. Rev. A* **83**, 053420 (2011).
- [45] Bilal, M. Pant, H. Zaheer, L. Garcia-Hernandez, and A. Abraham, Differential Evolution: A review of more than two decades of research, *Eng. Appl. Artif. Intell.* **90**, 103479 (2020).
- [46] M. F. Ahmad, N. A. M. Isa, W. H. Lim, and K. M. Ang, Differential Evolution: A recent review based on state-of-the-art works, *Alexandria Eng. J.* **61**, 3831 (2022).
- [47] N. Khaneja, T. Reiss, C. Kehlet, T. Schulte-Herbrüggen, and S. J. Glaser, Optimal control of coupled spin dynamics: design of NMR pulse sequences by gradient ascent algorithms, *J. Magn. Reson.* **172**, 296 (2005).
- [48] S. Machnes, U. Sander, S. J. Glaser, P. de Fouquières, A. Gruslys, S. Schirmer, and T. Schulte-Herbrüggen, Comparing, optimizing, and benchmarking quantum-control algorithms in a unifying programming framework, *Phys. Rev. A* **84**, 022305 (2011).
- [49] K.-X. Yan, Y. Qiu, Y. Xiao, Y.-H. Chen, and Y. Xia, Generating three-photon Rabi oscillations without a large-detuning condition, *Phys. Rev. A* **110**, 043711 (2024).
- [50] W. Shao, C. Wu, and X.-L. Feng, Generalized James' effective Hamiltonian method, *Phys. Rev. A* **95**, 032124 (2017).
- [51] C. K. Law, Interaction between a moving mirror and radiation pressure: A Hamiltonian formulation, *Phys. Rev. A* **51**, 2537 (1995).
- [52] V. Macrì, A. Ridolfo, O. Di Stefano, A. F. Kockum, F. Nori, and S. Savasta, Nonperturbative dynamical Casimir effect in optomechanical systems: Vacuum Casimir-Rabi splittings, *Phys. Rev. X* **8**, 011031 (2018).
- [53] S. S. Ivanov, B. T. Torosov, and N. V. Vitanov, High-fidelity quantum control by polychromatic pulse trains, *Phys. Rev. Lett.* **129**, 240505 (2022).
- [54] R. Storn and K. Price, Differential Evolution – a simple and efficient heuristic for global optimization over continuous spaces, *J. Global Optim.* **11**, 341 (1997).
- [55] S. Das and P. N. Suganthan, Differential Evolution: A survey of the state-of-the-art, *IEEE Trans. Evol. Comput.* **15**, 4 (2011).
- [56] R. H. Byrd, P. Lu, J. Nocedal, and C. Zhu, A limited memory algorithm for bound constrained optimization, *SIAM J. Sci. Comput.* **16**, 1190 (1995).
- [57] C. Zhu, R. H. Byrd, P. Lu, and J. Nocedal, Algorithm 778: L-BFGS-B: Fortran subroutines for large-scale bound-constrained optimization, *ACM Trans. Math. Softw.* **23**, 550 (1997).
- [58] J.-F. Huang and C. K. Law, Photon emission via vacuum-dressed intermediate states under ultrastrong coupling, *Phys. Rev. A* **89**, 033827 (2014).
- [59] R. Stassi, A. Ridolfo, O. Di Stefano, M. J. Hartmann, and S. Savasta, Spontaneous conversion from virtual to real photons in the ultrastrong-coupling regime, *Phys. Rev. Lett.* **110**, 243601 (2013).
- [60] A. Ridolfo, M. Leib, S. Savasta, and M. J. Hartmann, Photon blockade in the ultrastrong coupling regime, *Phys. Rev. Lett.* **109**, 193602 (2012).
- [61] V. E. Manucharyan, J. Koch, L. I. Glazman, and M. H. Devoret, Fluxonium: Single cooper-pair circuit free of charge offsets, *Science* **326**, 113 (2009).
- [62] C. W. S. Chang, C. Sabín, P. Forn-Díaz, F. Quijandría, A. M. Vadiraj, I. Nsanzineza, G. Johansson, and C. M. Wilson, Observation of three-photon spontaneous parametric down-conversion in a superconducting parametric cavity, *Phys. Rev. X* **10**, 011011 (2020).
- [63] M. Sandberg, C. M. Wilson, F. Persson, T. Bauch, G. Johansson, V. Shumeiko, T. Duty, and P. Delsing, Tuning the field in a microwave resonator faster than the photon lifetime, *Appl. Phys. Lett.* **92**, 203501 (2008).
- [64] L. B. Nguyen, Y.-H. Lin, A. Somoroff, R. Mencia, N. Grabon, and V. E. Manucharyan, High-coherence fluxonium qubit, *Phys. Rev. X* **9**, 041041 (2019).
- [65] L. Dania, D. S. Bykov, F. Goschin, M. Teller, A. Kassid, and T. E. Northup, Ultrahigh quality factor of a levitated nanomechanical oscillator, *Phys. Rev. Lett.* **132**, 133602 (2024).
- [66] I. Pietikäinen, O. Černotík, A. Eickbusch, A. Maiti, J. W. O. Garmon, R. Filip, and S. M. Girvin, Strategies and trade-offs for controllability and memory time of ultra-high-quality microwave cavities in circuit QED (2024), [arXiv:2403.02278 \[quant-ph\]](https://arxiv.org/abs/2403.02278).
- [67] C. P. Koch, U. Boscain, T. Calarco, G. Dirr, S. Filipp, S. J. Glaser, R. Kosloff, S. Montangero, T. Schulte-Herbrüggen, D. Sugny, and F. K. Wilhelm, Quantum optimal control in quantum technologies. strategic report on current status, visions and goals for research in Europe, *EPJ Quantum Technol.* **9**, 19 (2022).
- [68] F. Dolde, V. Bergholm, Y. Wang, I. Jakobi, B. Naydenov, S. Pezzagna, J. Meijer, F. Jelezko, P. Neumann, T. Schulte-Herbrüggen, J. Biamonte, and J. Wrachtrup, High-fidelity spin entanglement using optimal control, *Nat. Commun.* **5**, 3371 (2014).
- [69] V. Nebendahl, H. Häffner, and C. F. Roos, Optimal control of entangling operations for trapped-ion quantum computing, *Phys. Rev. A* **79**, 012312 (2009).